Reconstructing dual-phase nanometer scale grains within a pearlitic steel tip in 3D through 4D-scanning precession electron diffraction tomography and automated crystal orientation mapping

Patrick Harrison, Xuyang Zhou, Saurabh Mohan Das, Pierre Lhuissier, Christian H. Liebscher, Michael Herbig, Wolfgang Ludwig, Edgar F. Rauch

Reconstructing Dual-Phase Nanometer Scale Grains within a Pearlitic Steel Tip in 3D through 4D-Scanning Precession Electron Diffraction Tomography and Automated Crystal Orientation Mapping

Patrick Harrison*[1], Xuyang Zhou[2], Saurabh Mohan Das[2], Pierre Lhuissier[1], Christian H. Liebscher[2], Michael Herbig[2], Wolfgang Ludwig[3,4], Edgar F. Rauch[1]

[1] Univ. Grenoble Alpes, CNRS, Grenoble INP, SIMAP, F-38000 Grenoble, France

[2] Max-Planck-Institut für Eisenforschung, Max-Planck-Strasse 1, 40237 Düsseldorf, Germany

[3] ESRF – The European Synchrotron, Grenoble, France

[4] MATEIS, INSA Lyon, UMR 5510 CNRS, 25 av Jean Capelle, 69621 Villeurbanne, France

*Corresponding author, email: patrick.harrison@simap.grenoble-inp.fr

Abstract

The properties of polycrystalline materials are related to their microstructures and hence a complete description, including size, shape, and orientation of the grains, is necessary to understand the behaviour of materials. Here, we use Scanning Precession Electron Diffraction (SPED) in the Transmission Electron Microscope (TEM) combined with a tilt series to reconstruct individual grains in 3D within a polycrystalline dual-phase cold wire-drawn pearlitic steel sample. Nanoscale ferrite grains and

intragranular cementite particles were indexed using an Automated Crystallographic Orientation Mapping (ACOM) tool for each tilt dataset. The grain orientations were tracked through the tilt datasets and projections of the individual grains were reconstructed from the diffraction data using an orientation-specific Virtual Dark Field (VDF) approach for tomographic reconstruction. The algorithms used to process and reconstruct such datasets are presented. These algorithms represent an extension to the ACOM approach that may be straightforwardly applied to other multi-phase polycrystalline materials to enable 3D spatial and orientation reconstructions.

Keywords

Transmission Electron Microscopy (TEM), Scanning Precession Electron Diffraction (SPED), Automated Crystal Orientation Mapping (ACOM), Diffraction tomography, Pearlitic Steel, Nanoscale grains

1 Introduction

The microstructure of polycrystalline materials plays a role in determining the material properties such as ductility, hardness, and wear resistance [1]. Over the past 20 years, a variety of synchrotron X-ray based techniques have been developed to measure the 3-dimensional microstructure (see references [2,3] and references therein), however the spatial resolution is typically limited to ~1μm, and although this has been improved to ~100nm for recent variants [4,5], it remains insufficient to resolve nanoscale structures. Electron Backscatter Diffraction (EBSD) is commonly employed for surface orientation mapping and can be extended into three dimensions in combination with Focused Ion Beam (FIB) sectioning [6]. This technique, however, is destructive and the resolution is limited to tens of nanometers.

Scanning TEM (STEM) is a powerful tool for investigating nanomaterials and commonly achieves atomic resolution in imaging modes. TEM-based techniques have been developed to perform orientation mapping at the nanometer scale, notably the dark-field conical scanning [7,8] and scanning electron nanobeam diffraction techniques (NBD) [9,10]. In the latter, the electron beam is scanned over two dimensions across a specimen and a diffraction pattern is recorded at each probe position, resulting in 4-dimensional data. Due to strong dynamical effects associated with electron diffraction this technique is commonly extended to Scanning Precession Electron Diffraction [11,12]. Here, the electron beam is precessed through a small-angle hollow cone which probes more lattice points in reciprocal space. This reduces the measured dynamical scattering effects by averaging the diffraction signal over many different beam directions [13]. The crystal orientations may then be calculated from the set of recorded diffraction patterns using Automated Crystal Orientation Mapping, which utilizes diffraction template matching and is a well-trusted strategy for orientation and phase mapping in TEM [14]. The combination of both ACOM and precession is commonly employed as the use of precession improves the orientation resolution of the indexing procedure [15,16]. The resulting 2-dimensional orientation maps provide information about the sample microstructure, however some ambiguity as to the true through-thickness positions of the identified grains remain. Techniques have been further developed to separate information resulting from overlapping grains in transmission [17] and to reconstruct images of the grains from the set of diffraction patterns, known as virtual reconstruction [18].

Both TEM orientation mapping techniques outlined above have been extended to 3-dimensions by different groups. Liu et al. [19] applied the dark-field conical scanning technique 3D-OMiTEM to reconstruct the shapes and orientations of an aluminum sample. Eggeman et al. [20] utilized SPED combined with a tilt series, called Scanning Precession Electron Tomography (SPET), to image precipitates in a Ni-based superalloy. Their processing technique used the unsupervised machine learning technique non-negative matrix factorization (NMF) to classify the diffraction patterns obtained from the different phases in the sample. Whilst the non-negativity constraint imposed by NMF promotes physical interpretation of the solution components, the algorithm is sensitive to initialization methods [21] and is ill-suited to gradually changing features such as materials containing local misorientations

[20,22]. Meng and Zuo [23] used the virtual dark field (VDF) reconstruction method to reconstruct grains from their diffraction intensities. VDF reconstructions were created by integrating Bragg reflections which highlighted the same grain in real space and subsequently combined to create a final image of each grain. Both NMF and VDF methods have the advantage that they do not require prior knowledge of the crystal structure and have recently been further compared [22]. The reconstructed images of the grains at different tilt angles from the diffraction data were used as projections for tomographic reconstruction in both cases.

Here, we reconstruct grains of a pearlitic steel tip in three dimensions from SPED data using an expanded VDF technique that incorporates knowledge of the crystal orientation and phase. Manual selection of the Bragg reflections and subsequent comparison of the grain projections is a subjective and time-consuming procedure, thus we automate the selection of VDF apertures by using orientation and phase selective diffraction templates calculated through template matching. Cementite particles were identified using the same algorithms in the predominantly ferrite sample and subsequently reconstructed [24]. The orientation maps calculated from the tilt series datasets were coupled and used to track the grains in 3D for subsequent fiducial alignment.

2 Experimental

A pearlitic steel wire with composition Fe-0.98C-0.31Mn-0.20Si-0.20Cr (wt.%) was cold-drawn to a true strain of 6.5 and annealed for 2 min at 400°C was used as the material system [25] to conduct the method development. The cold-drawing process leads to a microstructure of columnar ferrite grains and the annealing to slight grain coarsening to a diameter of ~30 nm perpendicular to the columnar axis, as well as to carbon grain boundary segregation and the formation of spherical cementite [26]. This microstructure is ideally suited to establish the measurement approach as the grain orientations can be measured without significant grain overlap along the columnar direction. Further, this material system

is of interest because of its outstanding strength [27] that is linked to the segregation of carbon to its grain boundaries [25].

SPED experiments were performed using a JEOL JEM-2200FS electron microscope operated at 200 kV with a spot size of 1 nm and with 0.5º precession angle supplied by a Digistar hardware unit (NanoMEGAS SPRL). Each SPED dataset was acquired with a step size of 1.4 nm over a scan frame comprising (255 x 276) pixels at a frame rate of 24 frames per second. A Fischione Instruments Model 2050 On-Axis Rotation Tomography Holder was used to tilt the sample and SPED datasets were acquired at nine projection angles over 360º. At each applied tilt an Annular Dark Field (ADF) image was also acquired as a reference image, using a camera length of 25 cm. An Omega-type energy filter with a slit width equivalent of 30 eV was used to reduce the influence of inelastically scattered electrons and the diffraction patterns were recorded with a scintillator coupled CMOS (complementary metal-oxide-semiconductor) camera (TVIPS TemCam-XF416) at (512 x 512) pixels ((8 x 8) pixel binning). The data was processed using the ASTAR software package [14] (NanoMEGAS SPRL) and Python codes making use of the well-used NumPy [28] and SciPy [29] software stacks. ASTAR was used to calculate crystal orientations using both multi-indexing (5 indexing passes) and dual phase (α-Fe and cementite) approaches. Further orientation calculations were performed using the orix [30] library. Fiducial alignment was performed as implemented in the IMOD [31] software.

3 Processing

For polycrystalline materials such as the pearlitic steel tip presented here, an individual diffraction pattern may contain information constituted by many grains through the sample volume along the beam direction. The ACOM template matching algorithm will calculate the orientation from only the dominant grain within a given diffraction pattern despite this possibility. A multi-indexing strategy has been previously developed to characterize the information from overlapping grains [17]. Briefly, this involves iteratively calculating the optimum template for a given pattern multiple times. After each indexing pass,

the information within the diffraction pattern that was identified by optimum template is removed and the resulting 'reduced' pattern then undergoes another indexing pass to find the next dominant orientation. Performing this procedure for every diffraction pattern within the dataset results in multiple orientation maps which are combined into an orientation map stack as shown in SI 1. This procedure may be used to quantify grains and phases that would remain unidentified through a single indexing pass. An example is shown in Figure 1, which shows that the green grain near the sample apex would remain unidentified without the use of multi-indexing.

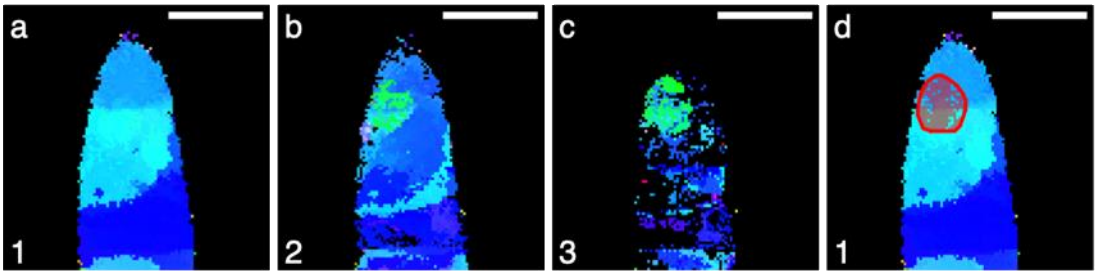

Figure 1: Multi-indexing reveals hidden grains in the pearlitic steel tip sample. (a-c) Orientation maps produced from the first three indexing passes, as indicated by the numbers inset. The grain with orientation close to (101) (green) is not recognized in the first indexing pass (a) but is identified in subsequent indexing passes (b-c). (d) The position of this grain overlaid in red on (a). The red line represents the convex hull of the grain and is shown for clarity. Black regions represent ignored values as determined by a lower threshold limit on the calculated correlation index. Colour map is the same as shown in Figure 6 and orientation maps were calculated from the 108.6° projection. Scale bars are 50 nm.

Pearlite is a dual-phase material consisting of lamellar ferrite (Fe, spacegroup 229, lattice parameter a=b=c=2.87 nm) and cementite (Fe_3C, spacegroup 62, lattice parameter a=5.09 nm, b=6.75 nm, c=4.52 nm), as such templates calculated from both phases were incorporated into the ACOM indexing strategy. The cementite phase was easily identified in the sample, as shown in SI 2, however the orientation reliability of the indexed cementite particles was low due to their small sizes and weak diffraction signals. As such the larger ferrite grains were used to align and process the datasets as discussed in the coming sections.

3.1 Frozen Template Virtual Dark Field

The recent rise in 4-dimensional scanning electron diffraction experiments has led to an increased importance of post-processing techniques. For scanning electron diffraction data this includes the use of virtual apertures [18,32] to highlight sample regions which possess a common diffracting signature. A virtual reconstruction is then performed by integrating the data contained in each diffraction pattern within the dataset underneath these virtual apertures. An example VDF reconstructed image is shown in Figure 2(a). In this case a Bragg reflection in the diffraction pattern was selected as a virtual aperture and the resulting VDF image highlights two individual grains.

An improved representation of the diffraction signature of a grain may be calculated using knowledge of the crystal orientation calculated with ACOM. Expanding on this, a full diffraction template, which is used in the ACOM indexing procedure, contains the predicted excited Bragg reflections. The projected positions of these Bragg reflections on the detector for a given crystal orientation are calculated and then used as virtual apertures. The resulting image is called a Frozen Template Virtual Dark Field (FTVDF) reconstruction [33] as the positions of the virtual apertures are fixed whilst integrating over the scanning pixels, despite the potentially varying orientation of the sample over the scan area. An example illustrating this calculation is shown in Figure 2(b), which shows that the reconstructed grain contour is much improved using FTVDF when compared to VDF as the calculation includes more of the diffracted beams, but also that the reconstruction is more specific to the crystal orientation from which the diffraction template was calculated.

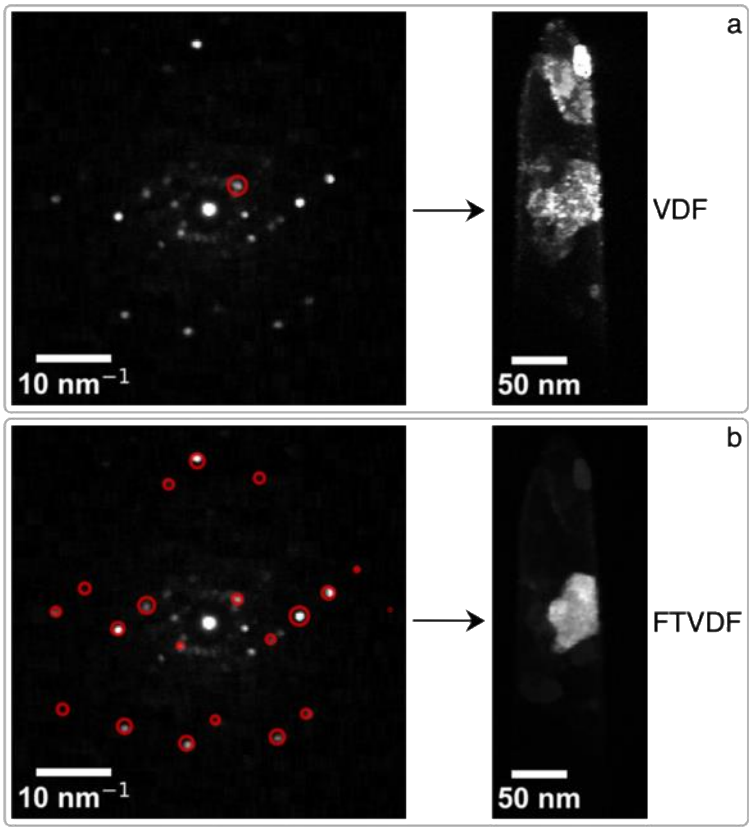

Figure 2: Calculation of (a) Virtual Dark Field (VDF) and (b) Frozen Template Virtual Dark Field (FTVDF) reconstructed images. The left column shows a selected experimental diffraction pattern. The virtual apertures used for the calculations in both cases are shown as red circles with radii proportional to the weight of each aperture. The right column shows the resulting reconstructed images.

3.2 Orientation Components

SPED datasets contain independent diffraction patterns which originate from the same grain and so a natural processing step is to cluster these patterns. Various methods, including diffraction pattern-based [22,34,35] and orientation-based [30,33] clustering, have been used to group and segment electron diffraction data. Here, the latter approach is used and a given orientation map is segmented into regions of similar orientation, which we call components. These components represent grains and are constructed by first calculating the disorientation matrix, the smallest misorientation after taking into account crystal symmetry operations, between all orientations within the orientation map and a given

orientation. Disorientation values smaller than a user-defined threshold, which should be larger than the observed intragranular orientation spread (nominally 5º), are segmented and labelled as a unique component. The initial reference orientations are chosen as those with the highest correlation index and this procedure happens automatically over the entire multi-indexed orientation map until all data points have been processed. The result is a labelled segmented map of grain components.

The overall projection of a grain may be better elucidated by combining multiple calculated orientation maps produced by multi-indexing. An example of this is shown in Figure 3. After the first orientation indexing pass the orange region (grain) in Figure 3(a-i) produces the calculated component in Figure 3(a-ii). However, the second indexing pass (Figure 3(b)) shows that this grain extends beyond its bounds as determined by the component calculated from the first pass. The combined component, shown in Figure 3(c), represents the projection of the grain more accurately. This observation is general to overlapping grains and inclined grain boundaries. The output from this procedure produces a binary mask of the grain, however an improved greyscale representation of the grain contour may be calculated using FTVDF which was introduced in 3.1 and will be discussed further in 3.4.

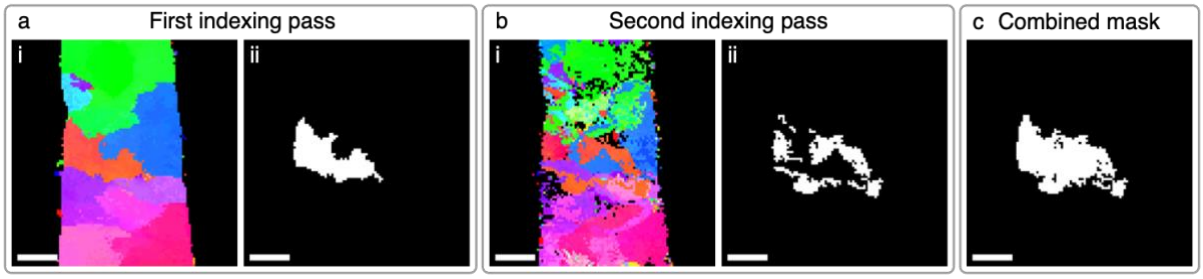

Figure 3: Schematic demonstrating the calculation of an individual component from a multiply-indexed orientation map. Orientation colour code is the same as shown in Figure 6. (i) Orientation maps and (ii) calculated components from the (a) first and (b) second indexing passes. Components were calculated using the same reference orientation in both (a) and (b). (c) The combined component (grain) mask calculated from (a(ii)) and (b(ii)). Scale bars are 25 nm.

The calculated components are then be filtered to remove erroneous data, such as few-pixel components which are typically noise originating from the indexing algorithm, and average statistics are calculated

for each component. The calculated components provide two benefits over full orientation maps: firstly, a reduction in data size from thousands of orientation data points to tens or hundreds of components and, secondly, calculation of the average grain orientations and centers of mass for each component, which may be used for orientation and real space alignment of the tilt series, respectively.

3.3 Orientation and Real Space Alignment

Whilst the rotation axis of the specimen holder in the electron microscope is known, this axis normally does not directly relate to the rotation of the diffraction pattern on the camera in the microscope, which is due to azimuthal rotation of the electron beam around the optical axis by the projector lenses. This rotation may is compensated in some microscopes or calibrated for a defined set of imaging parameters [36], however these calibrations may change over time. As a result, the rotation axis which couples the tilt series together must be calculated. An automatic approach to calculate this rotation vector (axis and angle) has been implemented.

The orientations o of components from tilt dataset i are coupled to the next tilt dataset $i+1$ by $o_{i+1} = ro_i$ where r is the rotation vector. The angle of r is known as it is the applied tilt to the specimen, whereas its axis within the reference frame of the calculated orientations is not known. This axis, however, typically has no vertical component as the applied rotations are confined to the specimen x-y (azimuthal) plane of the microscope. The disorientation between the datasets after applying symmetry operations then follows as $d = o_{i+1}(ro_i)^{-1}$. For two given tilt series orientations, small disorientations will always be calculated due to uncertainties in the applied rotation and the calculated orientations from orientation indexing. There is also the possibility of pattern misindexing due to the 180º ambiguity problem [37] which creates further complications for orientation coupling between tilt datasets, however algorithms have been developed to overcome this [33] and are employed here. On top of this it is also possible that the sets of orientations between tilt datasets are incomplete due to differing fields of view.

The disorientation matrix d is therefore calculated between all component orientations in each tilt dataset and the total cost of this matrix is determined by the solution to the minimum cost assignment problem [38], which assumes that an orientation in the first tilt dataset $o_{i,j}$ matches to only one orientation in the second tilt dataset $o_{i+1,k}$. The matching cost is therefore computed for many axis directions of r contained within the azimuthal plane of the diffraction patterns, and the axis direction with the lowest associated cost is chosen as the rotation vector which subsequently undergoes further refinement. An example calculation for this procedure is shown SI 4. The orientation data is then corrected such that tilts in both the real space and orientation space data occur around the same axis, which is the y-axis for the data presented here. This information therefore allows a component to be coupled between tilt datasets and tracked throughout the tilt series, as demonstrated by the {100} pole figure in Figure 4 for the grain presented in Figure 5. The accuracy of this method can be estimated from the spread of the calculated rotation vectors for the same microscope conditions; for the dataset presented here, the standard deviation of the set of their azimuthal angles is 0.4°.

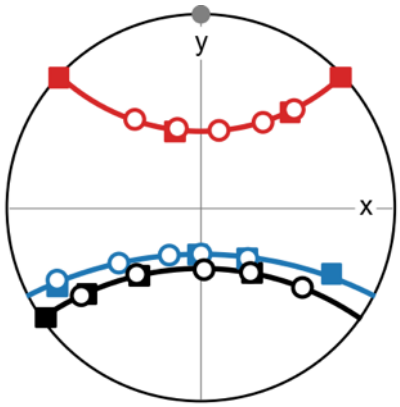

Figure 4: {100} pole figure of the ferrite grain presented in Figure 5 tracked throughout the tilt series. The measured component orientations at different tilts are shown as open circle and closed square datapoints for poles on the upper and lower hemispheres of the unit sphere, respectively. The corrected rotation axis is shown as a closed grey circle. The path of the calculated average orientation of the grain rotated around the rotation axis is shown as a line for each pole.

The tomographic reconstruction quality is limited by the alignment of the tilt series data amongst other factors, so it is necessary to calculate the proper alignment of the dataset. Initial coarse alignment and shear correction was performed by comparing the Virtual Bright Field (VBF) image reconstructed from each SPED dataset with the reference ADF image for each projection. Fiducial alignment algorithms have proven to be powerful tools for fine alignment [31] and are capable of linear and non-linear image distortion corrections which may be non-negligible in SPED datasets acquired over typical acquisition times of tens of minutes. The projected center of masses of each component were calculated for each tilt dataset and used as data points for real space fiducial fine alignment of the coarsely aligned SPED data.

3.4 Reconstruction

Projections of the individual grains were calculated using FTVDF, as shown in Figure 5. Not all grains could be unambiguously tracked through the dataset, as discussed above. In these cases a template created from an unambiguous orientation of a grain was rotated into the reference frames of the other tilt datasets and projections of the grain were computed using FTVDF from the simulated rotated template. The resulting images contain orientation-specific contrast of the grain of interest. It has been noticed that the grain contrast may be improved by refining the diffraction template on diffraction patterns originating from the highlighted grain of interest. Typically, the orientation of the refined template is around 1° from its initial orientation, which is an estimate of the total uncertainty of the calculated orientations and coupling rotations used in this work. As previously discussed, the low orientation reliability of the cementite phase means that it was not well-suited to FTVDF reconstruction. Cementite particles were identified using the calculated phase maps and VDF projections were calculated by manual selection of the Bragg reflections in the diffraction data.

The FTVDF intensities, reconstructed from diffracted beams, are affected by numerous factors, including dynamical diffraction, intragranular orientation gradients, and grain overlap. The effects of dynamical diffraction were reduced by beam precession during the experiment, whereas the latter two

effects are intrinsic to the sample and material studied. As a result, there are contrast fluctuations within each grain, which are visible in Figure 5, and, despite the use of precession, the FTVDF images do not exactly satisfy the projection criteria that the projected object intensity is proportional to the thickness of the object [39]. These effects, however, do not prevent a well-defined reconstruction of the grain contour.

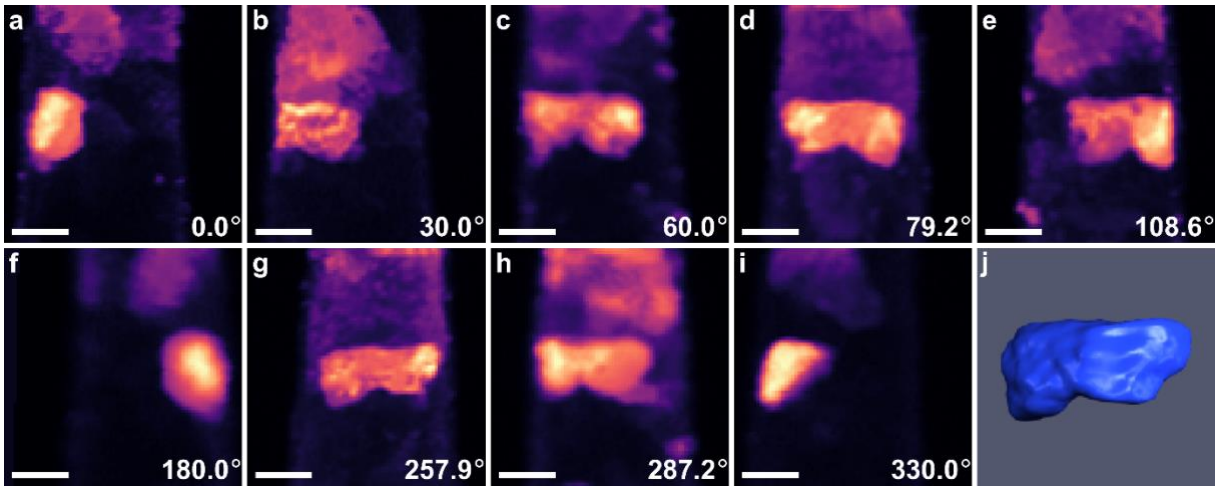

Figure 5: (a-i) FTVDF projections of an individual ferrite grain within the pearlitic steel tip. (j) 3D reconstructed isosurface rendering of the grain. Scale bars are 25 nm.

The total FTVDF intensity of each grain in each projection was normalized before tomographic reconstruction, under the assumption of a constant diffracting volume. Each grain was aligned using the global set of alignment parameters and reconstructed individually into a common volume using 25 iterations of the Simultaneous Iterative Reconstruction Technique (SIRT) combined with a non-negative minimum constraint to promote physical solutions [40]. The resulting combined rendering is provided as a video in SI 5 and shown in Figure 6 for two different projection angles. Figure 6(b) clearly shows that the grains are columnar along the drawing direction (z-axis), as expected from the preparation technique. The calculated orientation map obtained under the same projection is also presented in Figure 6(c). Comparison between Figure 6(b) and (c) demonstrates the extra information provided by 3D grain reconstruction. The positions and shapes of the grains are well defined in the 3D reconstruction whereas

in the 2D orientation map they are ambiguous in both two and three dimensions due to grain overlap. The hidden grain at the tip apex, discussed previously in section 3.2, is also absent from this orientation map, however its spatial position is well-defined in the 3D reconstruction. Furthermore, the cementite phase is identified within the sample (as depicted by the white arrow in Figure 6(c)), however the 3D reconstruction shows that these cementite particles are located on the far side of the sample and not in plane with other grains. These two artefacts arise from the dominant grain concept in the ACOM template matching procedure discussed previously. Further down the tip, the 2D orientation map shows regions of uncertain grain boundaries and shapes, for example the interface between the blue, orange, and purple grains which are oriented close to (111), (201), and (211), respectively. From the 2D orientation map it may interpreted that these three grains are located on the same z-y plane (x-y plane of the 2D orientation map), however the 3D reconstruction disproves this notion and shows that the grains exist at different x-positions within the sample. The knowledge of the relative positions of these grains is critical to further analysis of their grain boundary interfaces.

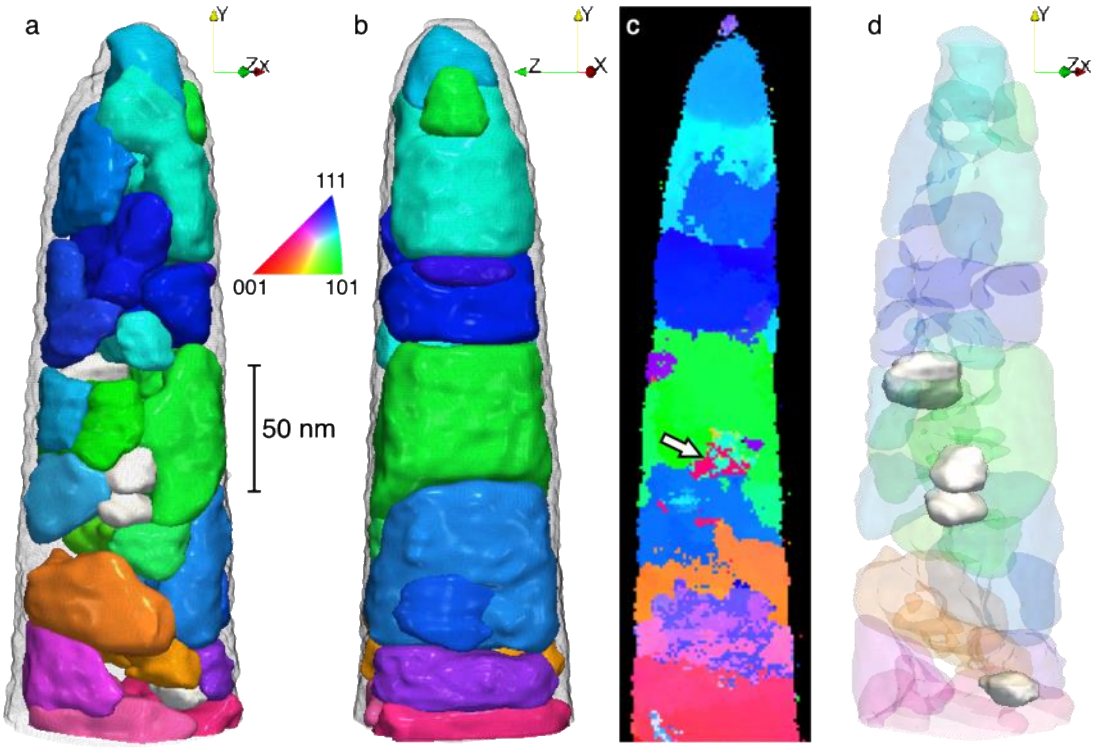

Figure 6: 3D reconstruction of the pearlitic steel tip projected (a) 30º and (b) 257.9º from the columnar direction of the grains (y-axis). Each grain is coloured by its average orientation projected along the length of the tip. Cementite particles are coloured white. ADF reconstruction also shown as a black isosurface wiremesh in (a) and (b). (c) The 2D calculated orientation map from the 257.9º projection. (d) The location of identified cementite particles within the tip, shown under the same projection as (a). A Gaussian filter with standard deviation of 1.4 nm (1 voxel) was applied to the reconstructed volumes during rendering.

Figure 6(d) highlights the locations and shapes of cementite particles that could be reconstructed from the dataset. The cementite particles are found at ferrite grain boundaries and have more spherical geometries when compared to the elongated columnar ferrite grains, which has been shown to be due to cementite growth during the annealing process [26]. Whilst the indexed cementite orientation is in general difficult to determine from a single diffraction pattern, under certain projections the indexed cementite displayed large, connected regions (>50 pixels, ~100 nm^2) of unchanging orientation, and the same orientations were also calculated under the reverse projection dataset (0º and 180º in this case), increasing the orientation reliability. Multiple planar $(001)_\theta \parallel (11\bar{2})_\alpha$ relationships between cementite particles and neighbouring ferrite grains were observed and are further detailed in SI 6. These represent

partial Bagaryatsky-type orientation relationships [41]. The lack of complete cementite-ferrite orientation relationship observed within the sample is likely due to the large amounts of plastic deformation within the sample due to the cold-drawing processing technique.

An ADF image was also recorded at each tilt position during the experiment. The ADF images were aligned using the cross-correlation technique and reconstructed using the SIRT algorithm with total variance minimization [42]. The resulting reconstruction is overlaid as a black mesh isosurface in Figure 6(a-b). The ADF reconstruction is considered as the reference reconstruction for the sample as the effects of sample drift in each ADF image are much reduced, when compared to the SPED scans, due to approximately two orders of magnitude decrease in scan time. The reconstructed grains are well contained within the ADF reconstruction, as expected, demonstrating the accuracy of the alignment of this diffraction tomography reconstruction technique. From the diffraction data there appears to be a thin (~5 nm) amorphous region surrounding the tip, which may be surface oxide species or have originated from the FIB milling process [43]. These regions remain unreconstructed by the diffraction technique and are consistent with the missing layer in the grain reconstruction when compared to the ADF reconstruction.

4 Discussion

The 3D-SPED technique presented here has been combined with ACOM to reliably track grains through the tilt series datasets and reconstruct projections of the grains using FTVDF. This reconstruction route was performed semi-automatically for the ferrite grains; manual input was required to adjust the FTVDF templates when the grains could not be reliably tracked throughout the tilt series, to improve the FTVDF reconstruction contrast, and for the fiducial alignment. The two former points are partially related to the material choice in this study, as the ferrite grains within the sample contained local misorientations due to plastic deformation caused by the cold-drawing technique. The total amount of manual input is expected to be less for more regular polycrystalline samples and it is anticipated that further algorithmic work will also contribute to this end.

Semi-automatic FTVDF reconstruction of the cementite particles was not possible due to their low orientation reliability, small sizes, and generally weak Bragg reflections. In future works on this material the experimental conditions could be further optimized to improve their diffraction signal, for example by increasing the exposure time, however this would come with a trade-off of sample damage and carbon contamination [44] associated with long beam exposure times.

The resolution of a tomographic reconstruction follows the Crowther criterion [45] and will improve with an increasing number of projections. For typical ADF tomography each image may take a few seconds to acquire, however each SPED scan acquired in this work took approximately 40 minutes and this puts a significant constraint on the number of projections that can be reasonably acquired by the microscope operator within the duration of a typical microscope user session. Recent improvements in camera speed and sensitivity [46] will offset this limitation. Despite this, new information, including the 3D grain position, size, and shape, are obtainable from the small number of scans (9) used in this work. This information cannot be properly resolved from a single 2D orientation map, nor from ADF tomography experiments due to the lack of observable contrast from differently oriented grains of the same phase.

The total reconstructed grain volume was calculated to be 78% of the reconstructed ADF volume as calculated by their convex hulls. Of this grain fraction 2% of the volume was identified as cementite, which would likely increase if all cementite particles in the sample could be reconstructed. The remaining unreconstructed volume apportioned to grain boundary regions, small grains, reconstruction errors, and ~10% of the unreconstructed volume is due to the unreconstructed amorphous layer, as discussed previously. Further analysis of the grain shapes is shown in SI 7 and confirms that the ferrite grains remain equiaxed perpendicular to the columnar axis and are also observed to have a <110> texture along their columnar axis (z-axis), in agreement with previous studies on this material system [25].

The ACOM technique has previously been combined with Atom Probe Tomography (APT) to study the effect of the chemical composition of the grain boundaries on grain misorientation [25]. While the investigation of grain boundary segregation with the existing approach, which combines NBD, ACOM, and APT, was limited to materials with columnar grains [25]. Future work is imagined involving the

combination of the 3D-SPED approach presented here with APT to investigate equiaxed nanocrystalline materials and with that to a significantly larger quantity of grain boundaries.

The material choice used in this work was optimal for the method development as there was limited grain overlap along the columnar direction, however the methods presented here are applicable to other materials. Potential limiting factors for successful reconstruction arise for materials containing small grains and those containing many grains through their projection. In the former case the grains will typically have weak diffracting intensity, which would be unsuitable for ACOM and VDF reconstruction, and in the latter case the multi-indexing strategy is not well suited to identifying more than 3-4 grains in a single diffraction pattern.

In general, this new approach will enable the investigation of all materials science events that involve local chemistry and crystallography in greater depth. To give one example, the nucleation of a new phase at a defect is affected by the combination of the crystallographic character of the defect and the local composition, an effect used for segregation engineering [47]. Interpretation of such processes are only possible if the full 3D information about crystallography and composition are available.

5 Conclusions

Here, we have demonstrated the 3D reconstruction of grains within a dual-phase polycrystalline pearlitic steel tip. By extending the ACOM technique into 3-dimensions, the final reconstruction provides information about the grain orientation, phase, and shape, which constitutes a full set of information for materials science applications. The orientation-based algorithms presented here are straightforwardly applicable to other materials of known phase. Future applications of this analysis and reconstruction method are envisaged to study grain boundaries at the nanoscale and complementary chemical analyses using APT.

6 References

[1] M.A. Meyers, A. Mishra, D.J. Benson, Mechanical properties of nanocrystalline materials, Progress in Materials Science. 51 (2006) 427–556. https://doi.org/10.1016/j.pmatsci.2005.08.003.

[2] A. Borbély, A.R. Kaysser-Pyzalla, X-ray diffraction microscopy: emerging imaging techniques for nondestructive analysis of crystalline materials from the millimetre down to the nanometre scale, J Appl Crystallogr. 46 (2013) 295–296. https://doi.org/10.1107/S0021889813004160.

[3] J.V. Bernier, R.M. Suter, A.D. Rollett, J.D. Almer, High-Energy X-Ray Diffraction Microscopy in Materials Science, Annu. Rev. Mater. Res. 50 (2020) 395–436. https://doi.org/10.1146/annurev-matsci-070616-124125.

[4] H.F. Poulsen, Multi scale hard x-ray microscopy, Current Opinion in Solid State and Materials Science. 24 (2020) 100820. https://doi.org/10.1016/j.cossms.2020.100820.

[5] Y. Hayashi, D. Setoyama, Y. Hirose, T. Yoshida, H. Kimura, Intragranular three-dimensional stress tensor fields in plastically deformed polycrystals, Science. 366 (2019) 1492–1496. https://doi.org/10.1126/science.aax9167.

[6] M. Calcagnotto, D. Ponge, E. Demir, D. Raabe, Orientation gradients and geometrically necessary dislocations in ultrafine grained dual-phase steels studied by 2D and 3D EBSD, Materials Science and Engineering: A. 527 (2010) 2738–2746. https://doi.org/10.1016/j.msea.2010.01.004.

[7] D.J. Dingley, Orientation Imaging Microscopy for the Transmission Electron Microscope, Microchim Acta. 155 (2006) 19–29. https://doi.org/10.1007/s00604-006-0502-4.

[8] G. Wu, S. Zaefferer, Advances in TEM orientation microscopy by combination of dark-field conical scanning and improved image matching, Ultramicroscopy. 109 (2009) 1317–1325. https://doi.org/10.1016/j.ultramic.2009.06.002.

[9] J.M. Cowley, Applications of electron nanodiffraction, Micron. 35 (2004) 345–360. https://doi.org/10.1016/j.micron.2003.12.002.

[10] A.S. Eggeman, Scanning transmission electron diffraction methods, Acta Crystallogr B Struct Sci Cryst Eng Mater. 75 (2019) 475–484. https://doi.org/10.1107/S2052520619006723.

[11] R. Vincent, P.A. Midgley, Double conical beam-rocking system for measurement of integrated electron diffraction intensities, Ultramicroscopy. 53 (1994) 271–282. https://doi.org/10.1016/0304-3991(94)90039-6.

[12] P.A. Midgley, A.S. Eggeman, Precession electron diffraction – a topical review, IUCrJ. 2 (2015) 126–136. https://doi.org/10.1107/S2052252514022283.

[13] P. Oleynikov, S. Hovmöller, X.D. Zou, Precession electron diffraction: Observed and calculated intensities, Ultramicroscopy. 107 (2007) 523–533. https://doi.org/10.1016/j.ultramic.2006.04.032.

[14] E.F. Rauch, M. Véron, Automated crystal orientation and phase mapping in TEM, Materials Characterization. 98 (2014) 1–9. https://doi.org/10.1016/j.matchar.2014.08.010.

[15] S. Nicolopoulos, D. Bultreys, E. Rauch, Precession coupled orientation/phase mapping on nanomaterials with TEM Cs microscopes, Acta Crystallogr A Found Crystallogr. 68 (2012) s104–s104. https://doi.org/10.1107/S0108767312097978.

[16] E.F. Rauch, M. Véron, Crystal Orientation Angular Resolution with Precession Electron Diffraction, Microscopy and Microanalysis. 22 (2016) 500–501. https://doi.org/10.1017/S1431927616003354.

[17] A. Valery, E.F. Rauch, A. Pofelski, L. Clement, F. Lorut, Dealing With Multiple Grains in TEM Lamellae Thickness for Microstructure Analysis Using Scanning Precession Electron Diffraction, Microscopy and Microanalysis. 21 (2015) 1243–1244. https://doi.org/10.1017/S143192761500700X.

[18] E.F. Rauch, M. Véron, Virtual dark-field images reconstructed from electron diffraction patterns, Eur. Phys. J. Appl. Phys. 66 (2014) 10701. https://doi.org/10.1051/epjap/2014130556.

[19] H.H. Liu, S. Schmidt, H.F. Poulsen, A. Godfrey, Z.Q. Liu, J.A. Sharon, X. Huang, Three-Dimensional Orientation Mapping in the Transmission Electron Microscope, Science. 332 (2011) 833–834. https://doi.org/10.1126/science.1202202.
[20] A.S. Eggeman, R. Krakow, P.A. Midgley, Scanning precession electron tomography for three-dimensional nanoscale orientation imaging and crystallographic analysis, Nat Commun. 6 (2015) 7267. https://doi.org/10.1038/ncomms8267.
[21] D. Kitamura, N. Ono, Efficient initialization for nonnegative matrix factorization based on nonnegative independent component analysis, 2016 IEEE International Workshop on Acoustic Signal Enhancement (IWAENC). (2016) 1–5. https://doi.org/10.1109/IWAENC.2016.7602947.
[22] T. Bergh, D.N. Johnstone, P. Crout, S. Høgås, P.A. Midgley, R. Holmestad, P.E. Vullum, A.T.J.V. Helvoort, Nanocrystal segmentation in scanning precession electron diffraction data, Journal of Microscopy. 279 (2020) 158–167. https://doi.org/10.1111/jmi.12850.
[23] Y. Meng, J.-M. Zuo, Three-dimensional nanostructure determination from a large diffraction data set recorded using scanning electron nanodiffraction, IUCrJ. 3 (2016) 300–308. https://doi.org/10.1107/S205225251600943X.
[24] P. Harrison, X. Zhou, S.M. Das, N. Viganò, P. Lhuissier, M. Herbig, W. Ludwig, E. Rauch, Reconstructing grains in 3D through 4D Scanning Precession Electron Diffraction, Microsc Microanal. 27 (2021) 2494–2495. https://doi.org/10.1017/S1431927621008898.
[25] M. Herbig, D. Raabe, Y.J. Li, P. Choi, S. Zaefferer, S. Goto, Atomic-Scale Quantification of Grain Boundary Segregation in Nanocrystalline Material, Phys. Rev. Lett. 112 (2014) 126103. https://doi.org/10.1103/PhysRevLett.112.126103.
[26] Y.J. Li, P. Choi, S. Goto, C. Borchers, D. Raabe, R. Kirchheim, Evolution of strength and microstructure during annealing of heavily cold-drawn 6.3GPa hypereutectoid pearlitic steel wire, Acta Materialia. 60 (2012) 4005–4016. https://doi.org/10.1016/j.actamat.2012.03.006.
[27] Y. Li, D. Raabe, M. Herbig, P.-P. Choi, S. Goto, A. Kostka, H. Yarita, C. Borchers, R. Kirchheim, Segregation Stabilizes Nanocrystalline Bulk Steel with Near Theoretical Strength, Phys. Rev. Lett. 113 (2014) 106104. https://doi.org/10.1103/PhysRevLett.113.106104.
[28] C.R. Harris, K.J. Millman, S.J. van der Walt, R. Gommers, P. Virtanen, D. Cournapeau, E. Wieser, J. Taylor, S. Berg, N.J. Smith, R. Kern, M. Picus, S. Hoyer, M.H. van Kerkwijk, M. Brett, A. Haldane, J.F. del Río, M. Wiebe, P. Peterson, P. Gérard-Marchant, K. Sheppard, T. Reddy, W. Weckesser, H. Abbasi, C. Gohlke, T.E. Oliphant, Array programming with NumPy, Nature. 585 (2020) 357–362. https://doi.org/10.1038/s41586-020-2649-2.
[29] SciPy 1.0 Contributors, P. Virtanen, R. Gommers, T.E. Oliphant, M. Haberland, T. Reddy, D. Cournapeau, E. Burovski, P. Peterson, W. Weckesser, J. Bright, S.J. van der Walt, M. Brett, J. Wilson, K.J. Millman, N. Mayorov, A.R.J. Nelson, E. Jones, R. Kern, E. Larson, C.J. Carey, İ. Polat, Y. Feng, E.W. Moore, J. VanderPlas, D. Laxalde, J. Perktold, R. Cimrman, I. Henriksen, E.A. Quintero, C.R. Harris, A.M. Archibald, A.H. Ribeiro, F. Pedregosa, P. van Mulbregt, SciPy 1.0: fundamental algorithms for scientific computing in Python, Nat Methods. 17 (2020) 261–272. https://doi.org/10.1038/s41592-019-0686-2.
[30] J. D. N., M. B. H., C. P, M. P. A., E. A. S., Density-based clustering of crystal (mis)orientations and the orix Python library, Journal of Applied Crystallography. 53 (2020) 1293–1298. https://doi.org/10.1107/S1600576720011103.
[31] D.N. Mastronarde, Fiducial Marker and Hybrid Alignment Methods for Single- and Double-axis Tomography, in: J. Frank (Ed.), Electron Tomography, Springer New York, New York, NY, 2006: pp. 163–185. https://doi.org/10.1007/978-0-387-69008-7_6.
[32] C. Gammer, V. Burak Ozdol, C.H. Liebscher, A.M. Minor, Diffraction contrast imaging using virtual apertures, Ultramicroscopy. 155 (2015) 1–10. https://doi.org/10.1016/j.ultramic.2015.03.015.
[33] E.F. Rauch, P. Harrison, X. Zhou, M. Herbig, W. Ludwig, M. Véron, New Features in Crystal Orientation and Phase Mapping for Transmission Electron Microscopy, Symmetry. 13 (2021) 1675. https://doi.org/10.3390/sym13091675.
[34] M. Gallagher-Jones, C. Ophus, K.C. Bustillo, D.R. Boyer, O. Panova, C. Glynn, C.-T. Zee, J. Ciston, K.C. Mancia, A.M. Minor, J.A. Rodriguez, Nanoscale mosaicity revealed in peptide microcrystals by scanning electron nanodiffraction, Commun Biol. 2 (2019) 26. https://doi.org/10.1038/s42003-018-0263-8.

[35] B.H. Martineau, D.N. Johnstone, A.T.J. van Helvoort, P.A. Midgley, A.S. Eggeman, Unsupervised machine learning applied to scanning precession electron diffraction data, Adv Struct Chem Imag. 5 (2019) 3. https://doi.org/10.1186/s40679-019-0063-3.
[36] G.J.C. Carpenter, Image and Diffraction Pattern Rotations in the TEM, Micros. Today. 20 (2012) 52–55. https://doi.org/10.1017/S1551929512000697.
[37] A. Morawiec, E. Bouzy, On the reliability of fully automatic indexing of electron diffraction patterns obtained in a transmission electron microscope, J Appl Cryst. 39 (2006) 101–103. https://doi.org/10.1107/S0021889805032966.
[38] D.F. Crouse, On implementing 2D rectangular assignment algorithms, IEEE Transactions on Aerospace and Electronic Systems. 52 (2016) 1679–1696. https://doi.org/10.1109/TAES.2016.140952.
[39] S. Hata, H. Furukawa, T. Gondo, D. Hirakami, N. Horii, K.-I. Ikeda, K. Kawamoto, K. Kimura, S. Matsumura, M. Mitsuhara, H. Miyazaki, S. Miyazaki, M.M. Murayama, H. Nakashima, H. Saito, M. Sakamoto, S. Yamasaki, Electron tomography imaging methods with diffraction contrast for materials research, Microscopy. 69 (2020) 141–155. https://doi.org/10.1093/jmicro/dfaa002.
[40] P. Gilbert, Iterative methods for the three-dimensional reconstruction of an object from projections, Journal of Theoretical Biology. 36 (1972) 105–117. https://doi.org/10.1016/0022-5193(72)90180-4.
[41] P.-Y. Tung, X. Zhou, D. Mayweg, L. Morsdorf, M. Herbig, Under-stoichiometric cementite in decomposing binary Fe-C pearlite exposed to rolling contact fatigue, Acta Materialia. 216 (2021) 117144. https://doi.org/10.1016/j.actamat.2021.117144.
[42] B. Goris, T. Roelandts, K.J. Batenburg, H. Heidari Mezerji, S. Bals, Advanced reconstruction algorithms for electron tomography: From comparison to combination, Ultramicroscopy. 127 (2013) 40–47. https://doi.org/10.1016/j.ultramic.2012.07.003.
[43] M. Herbig, A. Kumar, Removal of hydrocarbon contamination and oxide films from atom probe specimens, Microsc Res Tech. 84 (2021) 291–297. https://doi.org/10.1002/jemt.23587.
[44] A.E. Ennos, The origin of specimen contamination in the electron microscope, Br. J. Appl. Phys. 4 (1953) 101–106. https://doi.org/10.1088/0508-3443/4/4/302.
[45] R.A. Crowther, D.J. DeRosier, A. Klug, The reconstruction of a three-dimensional structure from projections and its application to electron microscopy, Proc. R. Soc. Lond. A. 317 (1970) 319–340. https://doi.org/10.1098/rspa.1970.0119.
[46] I. MacLaren, E. Frutos-Myro, D. McGrouther, S. McFadzean, J.K. Weiss, D. Cosart, J. Portillo, A. Robins, S. Nicolopoulos, E. Nebot del Busto, R. Skogeby, A Comparison of a Direct Electron Detector and a High-Speed Video Camera for a Scanning Precession Electron Diffraction Phase and Orientation Mapping, Microsc Microanal. 26 (2020) 1110–1116. https://doi.org/10.1017/S1431927620024411.
[47] D. Raabe, M. Herbig, S. Sandlöbes, Y. Li, D. Tytko, M. Kuzmina, D. Ponge, P.-P. Choi, Grain boundary segregation engineering in metallic alloys: A pathway to the design of interfaces, Current Opinion in Solid State and Materials Science. 18 (2014) 253–261. https://doi.org/10.1016/j.cossms.2014.06.002.

7 Funding Information

P.H. and E.F.R. would like to recognise funding from the Agence Nationale de la Recherche (grant no. ANR-19-CE42-0017). M.H. and S.M.D acknowledge funding by the German Research Foundation (DFG) via project H ANR-19-CE42-0017E 7225/11-1. X. Z. is supported by the Alexander von Humboldt Stiftung.

559

560 # 8 Competing Interests

561 The authors declare no competing interests.

562

Supporting Information

Reconstructing Dual-Phase Nanometer Scale Grains within a Pearlitic Steel Tip in 3D through 4D-Scanning Precession Electron Diffraction Tomography and Automated Crystal Orientation Mapping

Patrick Harrison*[1], Xuyang Zhou[2], Saurabh Mohan Das[2], Pierre Lhuissier[1], Christian H. Liebscher[2], Michael Herbig[2], Wolfgang Ludwig[3,4], Edgar F. Rauch[1]

[1] SIMAP Laboratory, CNRS-Grenoble INP, BP 46 101 rue de la Physique, 38402 Saint Martin d'Hères, France

[2] Max-Planck-Institut für Eisenforschung, Max-Planck-Strasse 1, 40237 Düsseldorf, Germany

[3] ESRF – The European Synchrotron, Grenoble, France

[4] MATEIS, INSA Lyon, UMR 5510 CNRS, 25 av Jean Capelle, 69621 Villeurbanne, France

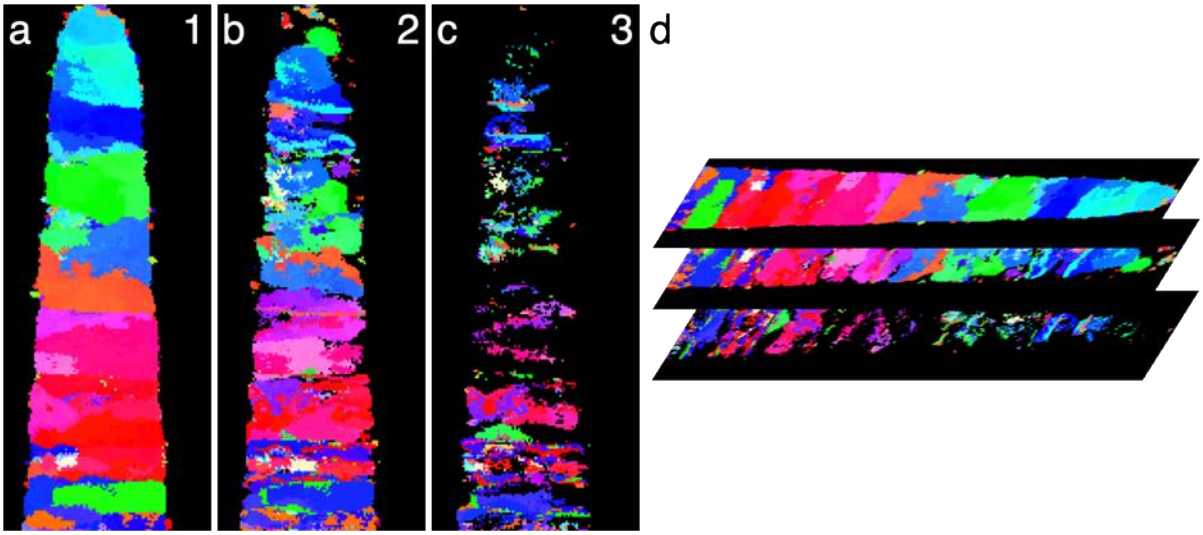

SI 1: Multi-indexing strategy example and strategy example taken from the 60° tilt dataset. (a-c) Raw orientation maps after 1, 2, and 3 indexing passes, respectively. Black pixels are masked by using a minimum threshold on the calculated correlation index. (d) These three maps (a-c) constitute a spatially aligned orientation map stack which is used for further processing, such as grain component calculation as discussed in section 3.2.

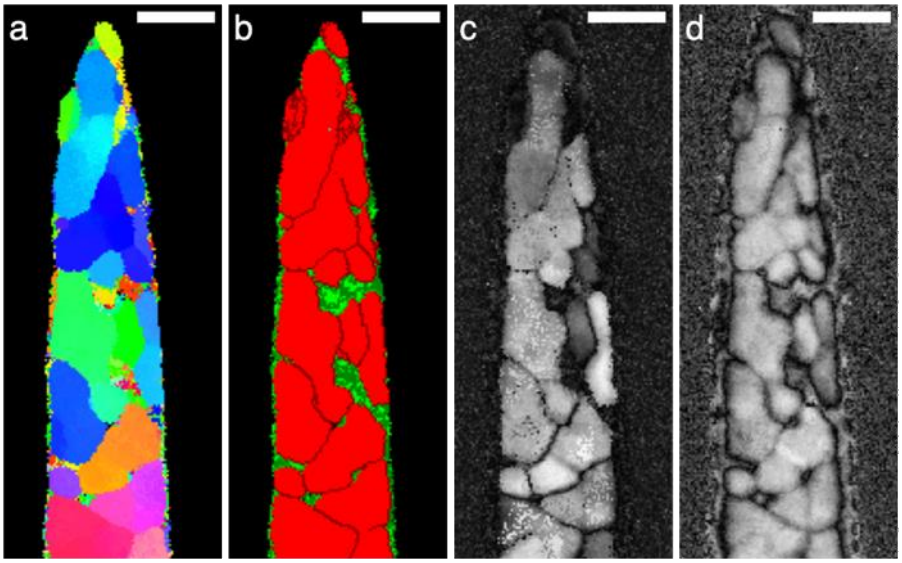

SI 2: (a) Calculated orientation map and (b) combined phase and grain boundary map for 180º projection. Ferrite and cementite phases are shown as red and green, respectively, in (b). (c) Associated orientation and (d) phase reliability maps. These maps combined show that the cementite phase is reliably indexed, but that the cementite orientation is not well defined. Note that the black pixels represent masked regions in (a) and (b) as determined by an orientation index threshold. Scalebars are 50 nm.

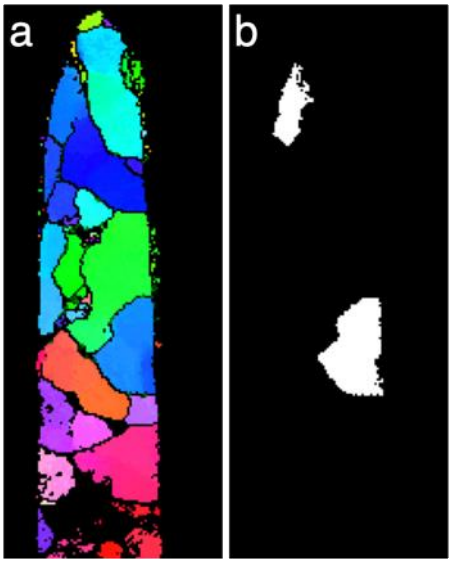

SI 3: Spatial separation of grain components. (a) Combined orientation and grain boundary map acquired from the 0° tilt dataset. The multi-indexed orientation stack is reduced to components through orientation-based clustering. In each dataset there is the possibility that spatially unconnected grains ae assigned to the same component. This is the case as shown in (b), the orientation clustering assigns the two white regions to the same component. In all cases the spatial information about each component is used to separate any spatially unconnected regions with similar orientation into multiple separated components.

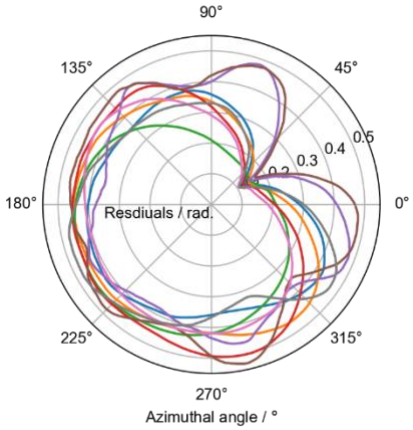

SI 4: Illustration of the calculation of the microscope rotation axis as described in the main text. The total coupled disorientation between adjacent tilt datasets i and $i+1$ is calculated after rotating tilt dataset i around a rotation axis r contained within the azimuthal plane. This residual disorientation is calculated for many directions of r positions around a full azimuthal rotation. The total residual exhibits a strong minimum when the rotation axis is correctly defined. Each coloured line represents the coupling residuals for different adjacent tilt datasets.

SI 5: Video. Pearlitic steel tip 3D rendering orbit.avi

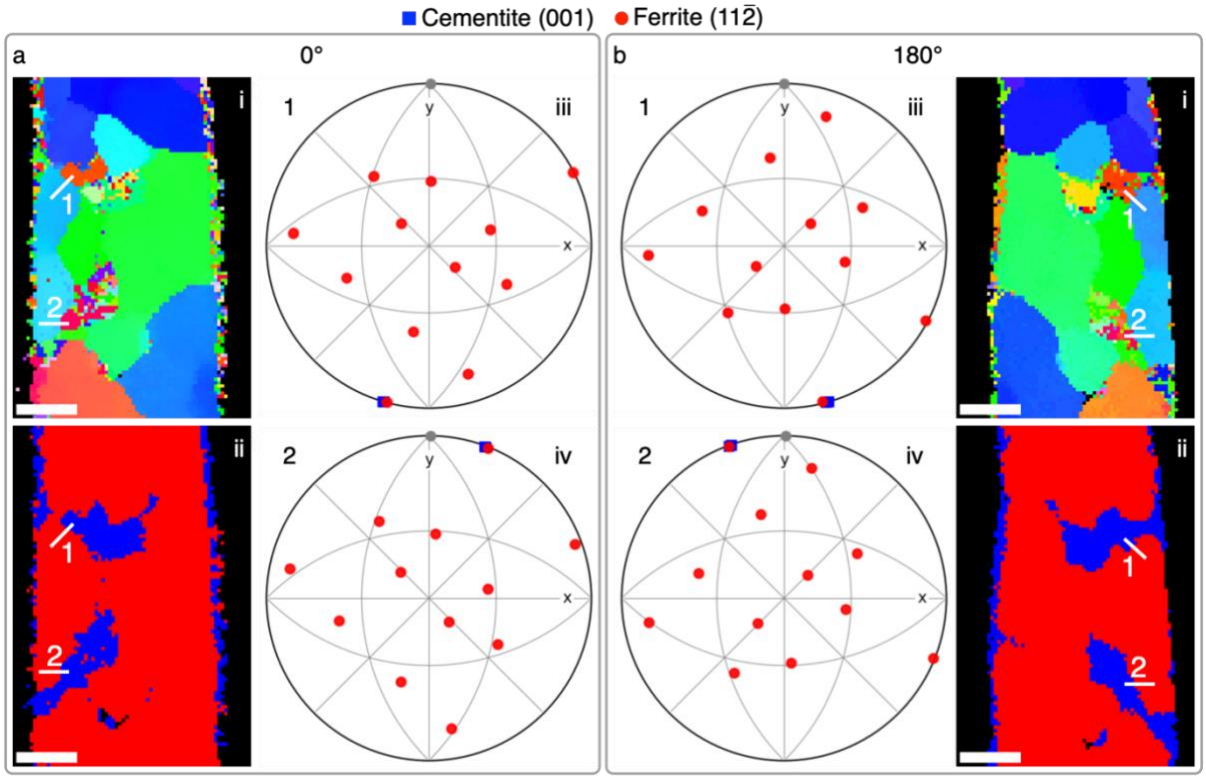

SI 6: Cementite-ferrite orientation relationships observed in the pearlitic steel tip. The indexed diffraction patterns at 0º and 180º (parallel to the drawing-direction) have the highest orientation reliabilities of all tilt datasets, this is due to increased grain overlap away from the columnar direction. (i) Orientation map, (ii) phase map, (iii) and (iv) pole figures extracted from line profiles 1 and 2, respectively, for the same grains under the (a) 0º and (b) 180º projection. In (ii-iv) the cementite and ferrite phases are shown as blue and red, respectively. Cementite (001) poles and ferrite (11$\bar{2}$) poles are shown in (iii) and (iv) as blue squares and red circles, respectively. Scale bars are 25 nm.

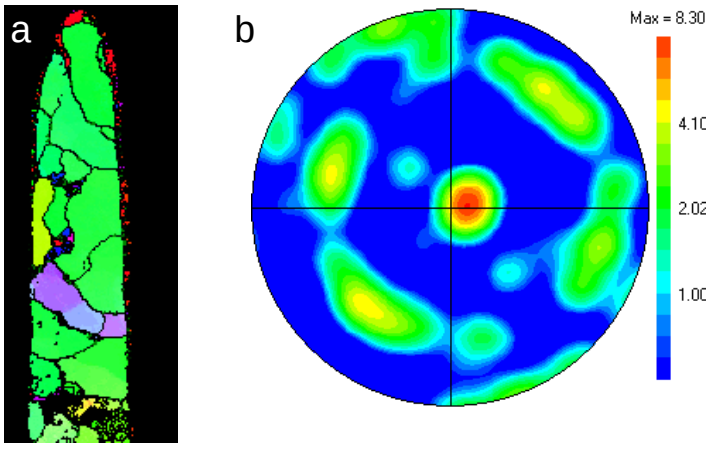

SI 7: (a) Orientation and grain boundary map for the 0º projection, which is parallel to the drawing direction (z-axis, Figure 6). The ferrite grains have a <110> texture along the drawing direction. Orientation colour codes are the same as in Figure 6. (b) <110> pole figure calculated from (a) with colours mapped onto a log scale.

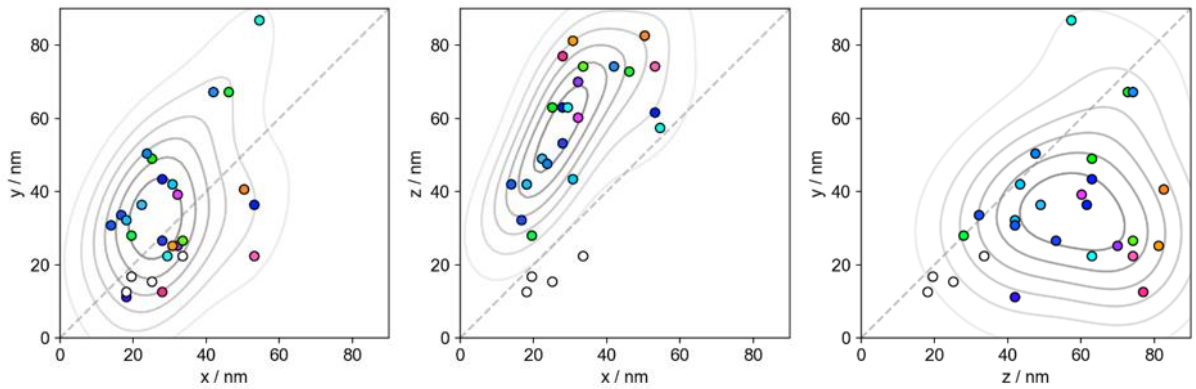

SI 8: Grain size distributions along all three pairs of axes (a) x-y, (b) x-z, and (c) y-z. Grain extents were calculated from their convex hulls. Contour plots show the size distribution as calculated from the kernel density estimate of the ferrite grain size distribution. The dashed line represents the expected trend for equiaxed grains. Datapoints are coloured by their orientation colour codes as shown Figure 6. The ferrite grains remain equiaxed perpendicular to the drawing direction (z-axis, Figure 6) and are elongated along the drawing direction.